REPORT DOCUMENTATION PAGE

Form Approved OMB No. 0704-0188

1. REPORT DATE *(DD-MM-YYYY)*	2. REPORT TYPE	3. DATES COVERED *(From - To)*
	Technical Papers	

4. TITLE AND SUBTITLE

5a. CONTRACT NUMBER

5b. GRANT NUMBER

5c. PROGRAM ELEMENT NUMBER

6. AUTHOR(S)

5d. PROJECT NUMBER
1011

5e. TASK NUMBER
CA9F

5f. WORK UNIT NUMBER

7. PERFORMING ORGANIZATION NAME(S) AND ADDRESS(ES)

Air Force Research Laboratory (AFMC)
AFRL/PRS
5 Pollux Drive
Edwards AFB CA 93524-7048

8. PERFORMING ORGANIZATION REPORT

9. SPONSORING / MONITORING AGENCY NAME(S) AND ADDRESS(ES)

Air Force Research Laboratory (AFMC)
AFRL/PRS
5 Pollux Drive
Edwards AFB CA 93524-7048

10. SPONSOR/MONITOR'S ACRONYM(S)

11. SPONSOR/MONITOR'S NUMBER(S)

12. DISTRIBUTION / AVAILABILITY STATEMENT

Approved for public release; distribution unlimited.

13. SUPPLEMENTARY NOTES

14. ABSTRACT

20030121 115

15. SUBJECT TERMS

16. SECURITY CLASSIFICATION OF:			17. LIMITATION OF ABSTRACT	18. NUMBER OF PAGES	19a. NAME OF RESPONSIBLE PERSON
a. REPORT	b. ABSTRACT	c. THIS PAGE			Leilani Richardson
Unclassified	Unclassified	Unclassified	A		19b. TELEPHONE NUMBER *(include area code)* (661) 275-5015

18 separate items enclosed

10 NOV 98

TP-1998-101

MEMORANDUM FOR IN-HOUSE PUBLICATIONS

FROM: PROI (TI) (STINFO) 7 May 98

SUBJECT: Authorization for Release of Technical Information, Control Number: AFRL-PR-ED-**TP**-1998-**101**

D.T. Baron, T.C. Miller, C.T. Liu "Subcritical Crack Growth in a Composite Solid Propellant"

Raytheon SPARTA PSM **PRESENTATION** ONLY **(Statement A)**

PHONE # 55790

DANIEL BARON
RAYTHEON STX

PRESENTATION ON 06-01-98
AT 1998 SOCIETY FOR EXPERIMENTAL MECHANICS (SEM)
SPRING CONFERENCE & EXPOSITION
HOUSTON, TX

Subcritical Crack Growth in a Composite Solid Propellant

D.T. Baron
Raytheon STX Corp.
Edwards AFB, CA

T.C. Miller
Sparta Inc.
Edwards AFB, CA

C.T. Liu
Air Force Research Laboratory
Edwards AFB, CA

b = 1.0 in., Crack Tip Blunting

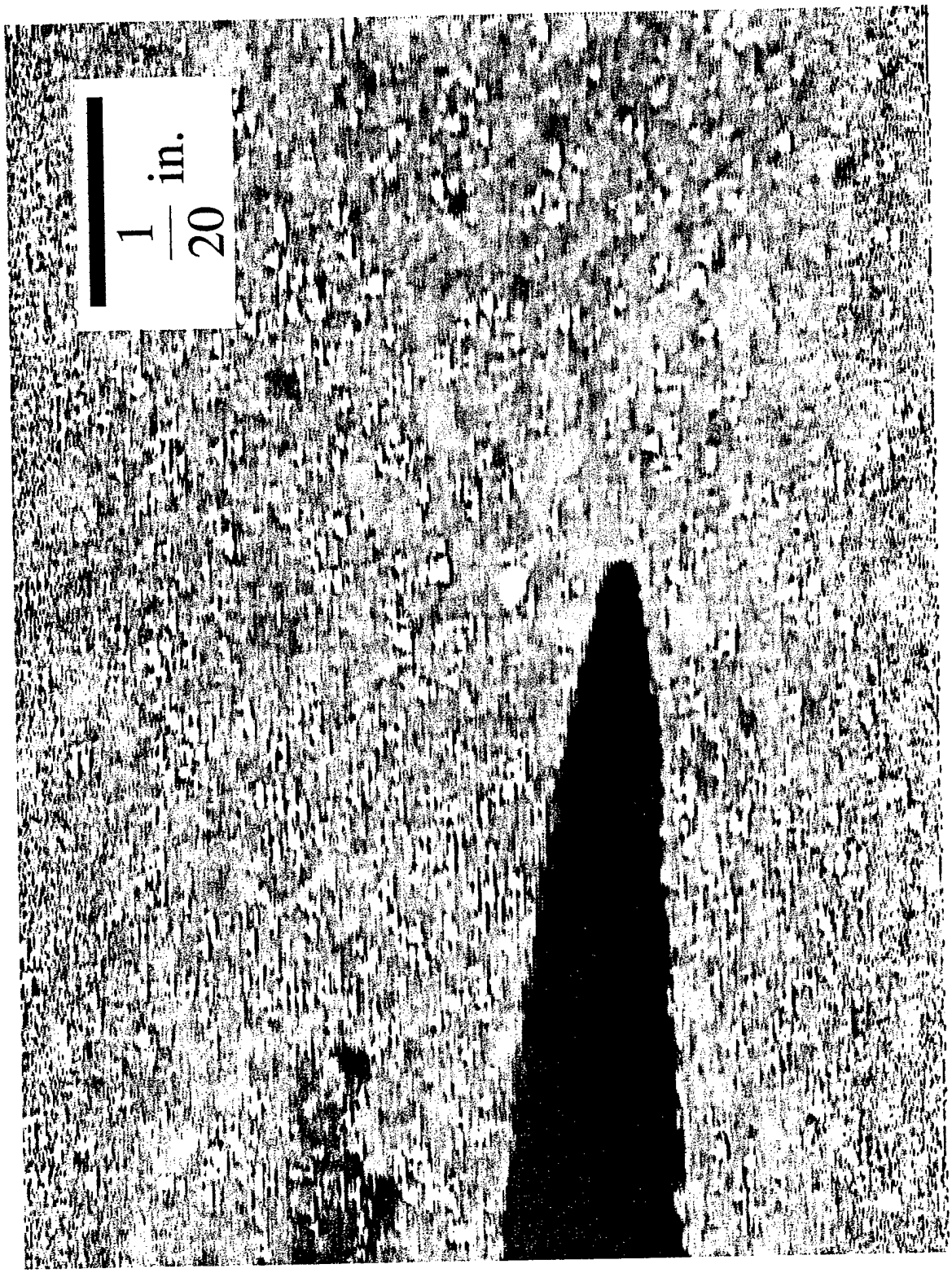

b = 1.0 in., Initial Crack Growth

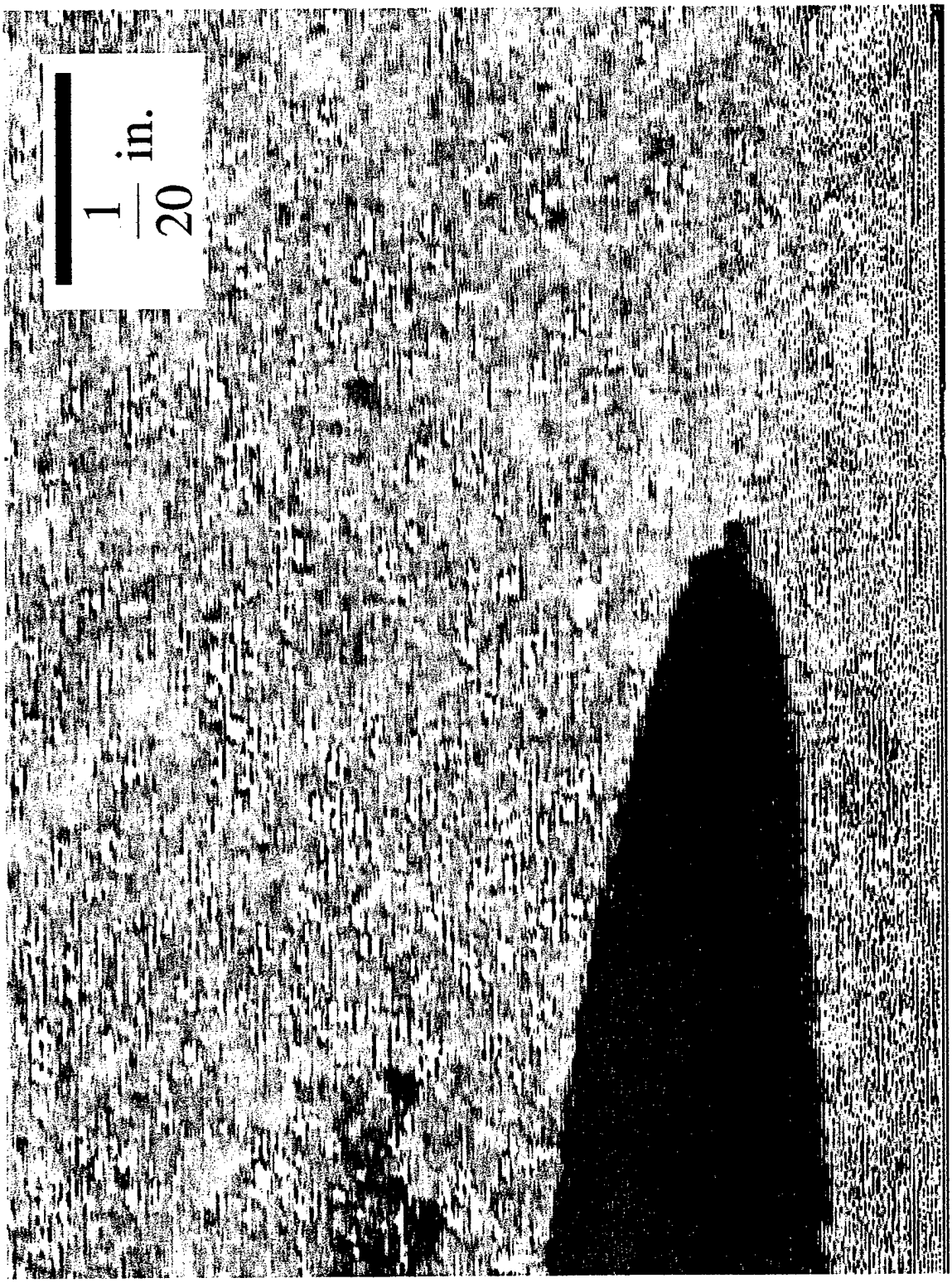

b = 1.5 in., Damage Formation

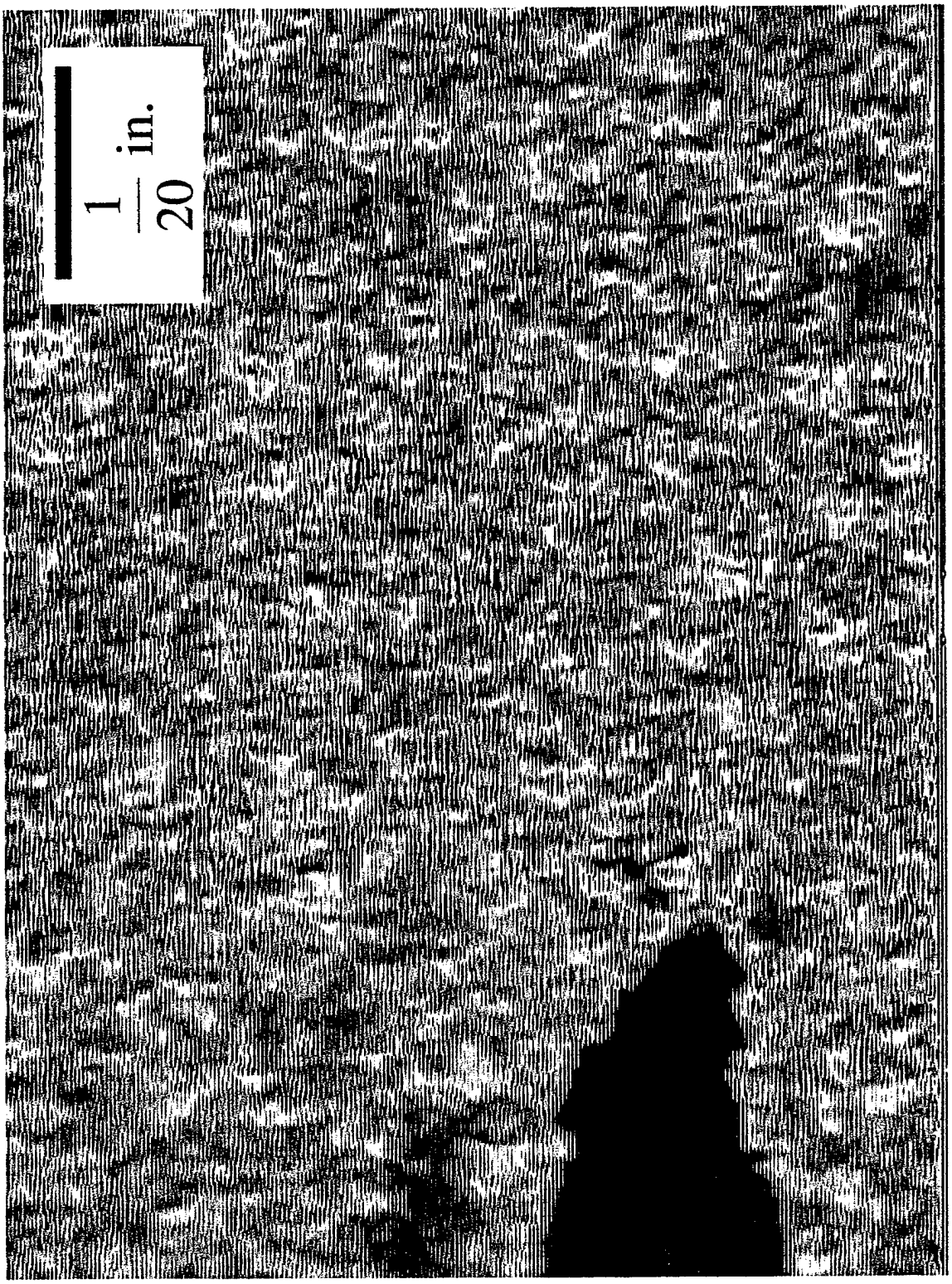

b = 0.2 in., Damage Zone Voids

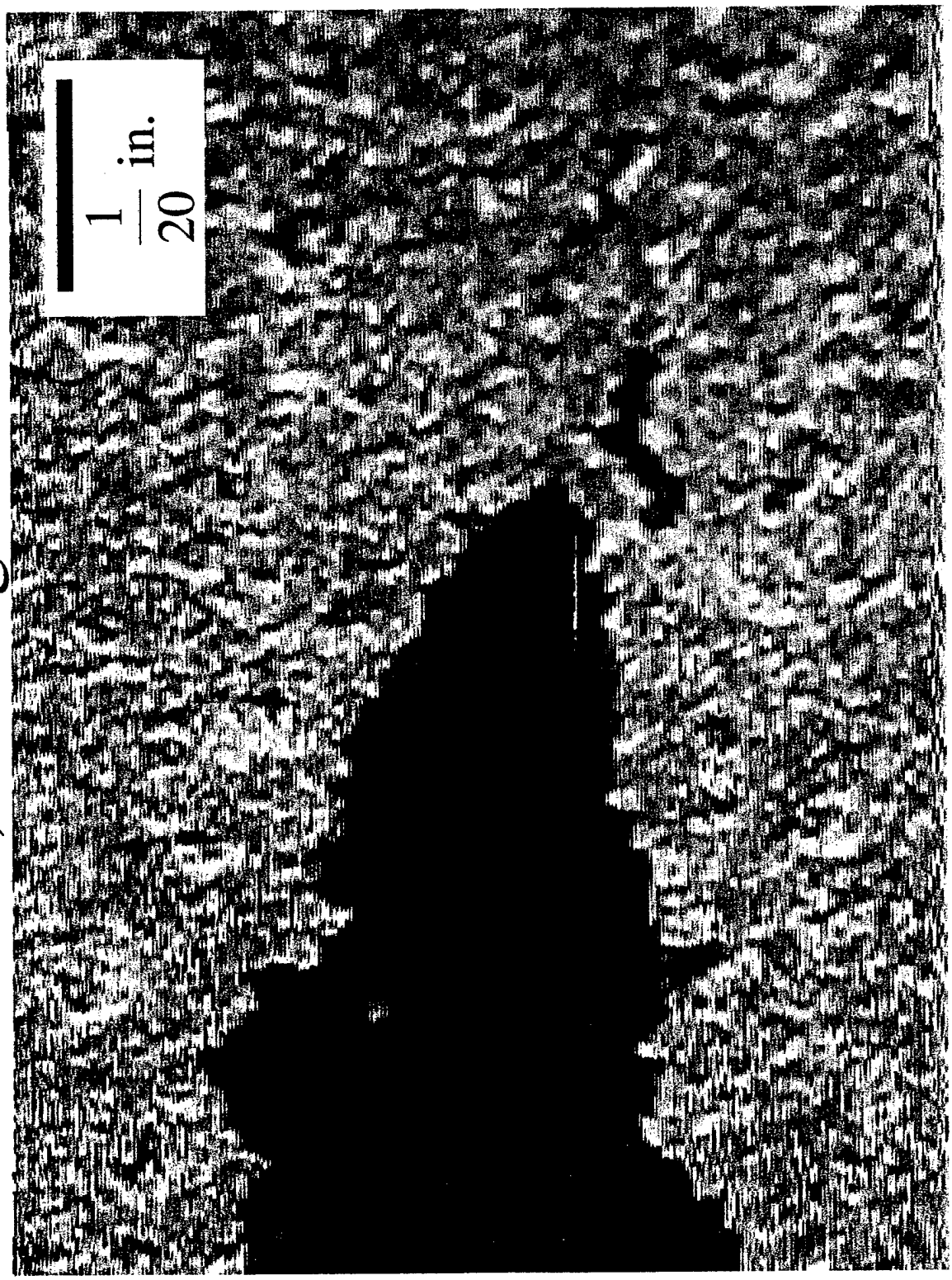

b = 0.2 in., Single Ligament

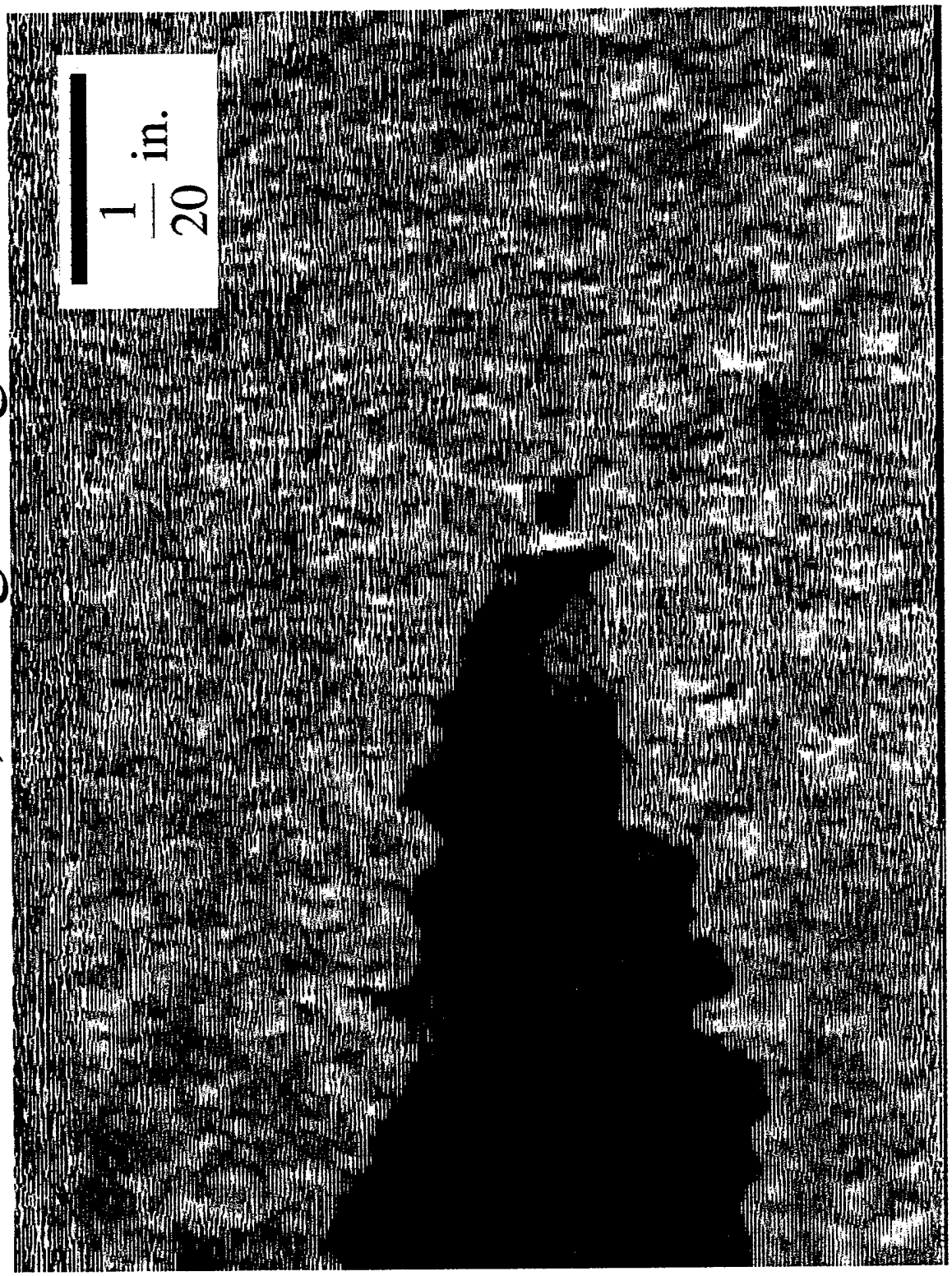

b = 0.5 in., Double Ligament

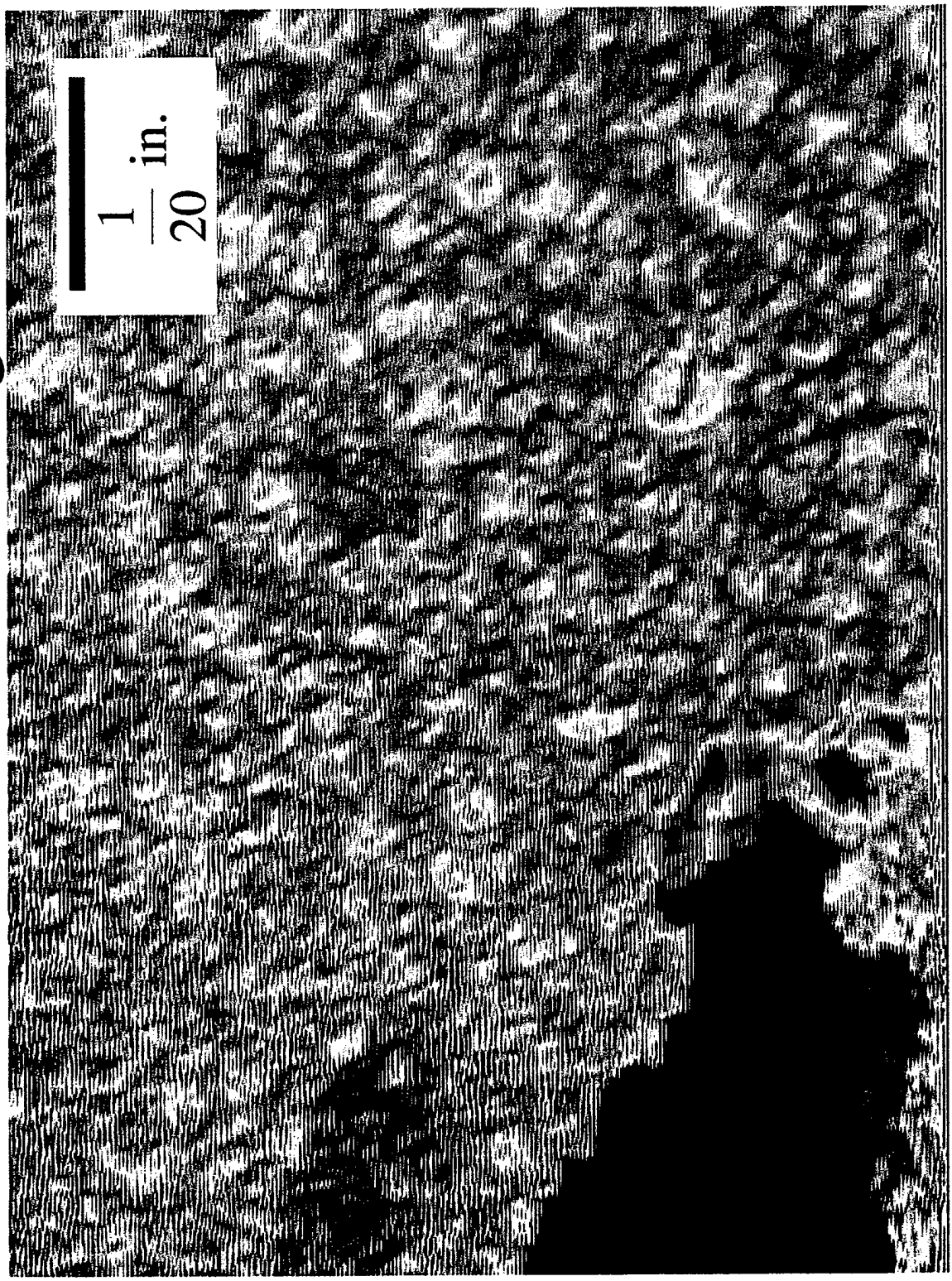

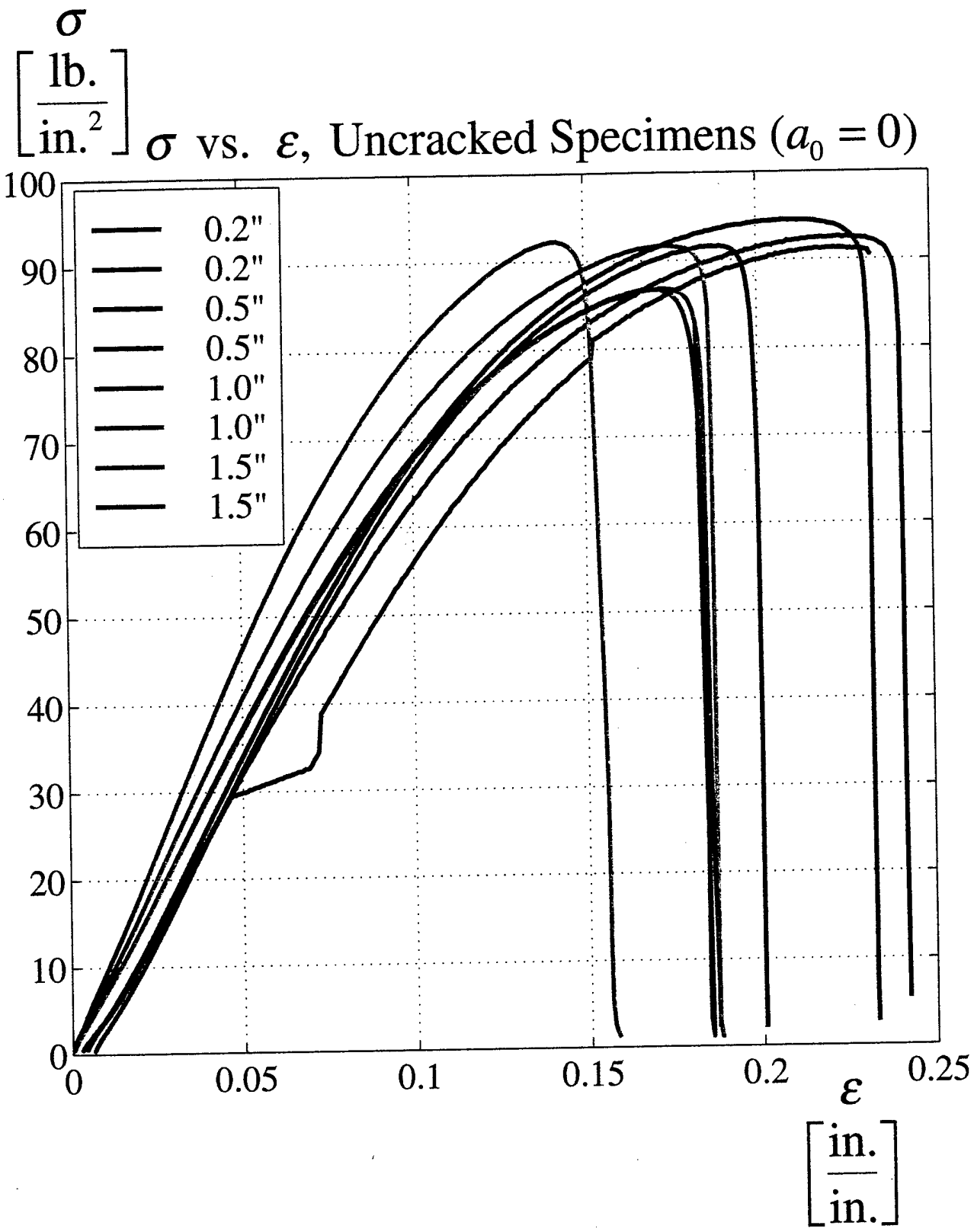
σ [lb./in.²]
σ vs. ε, Uncracked Specimens ($a_0 = 0$)
0.2"
0.2"
0.5"
0.5"
1.0"
1.0"
1.5"
1.5"
100
90
80
70
60
50
40
30
20
10
0
0
0.05
0.1
0.15
0.2
0.25
ε [in./in.]

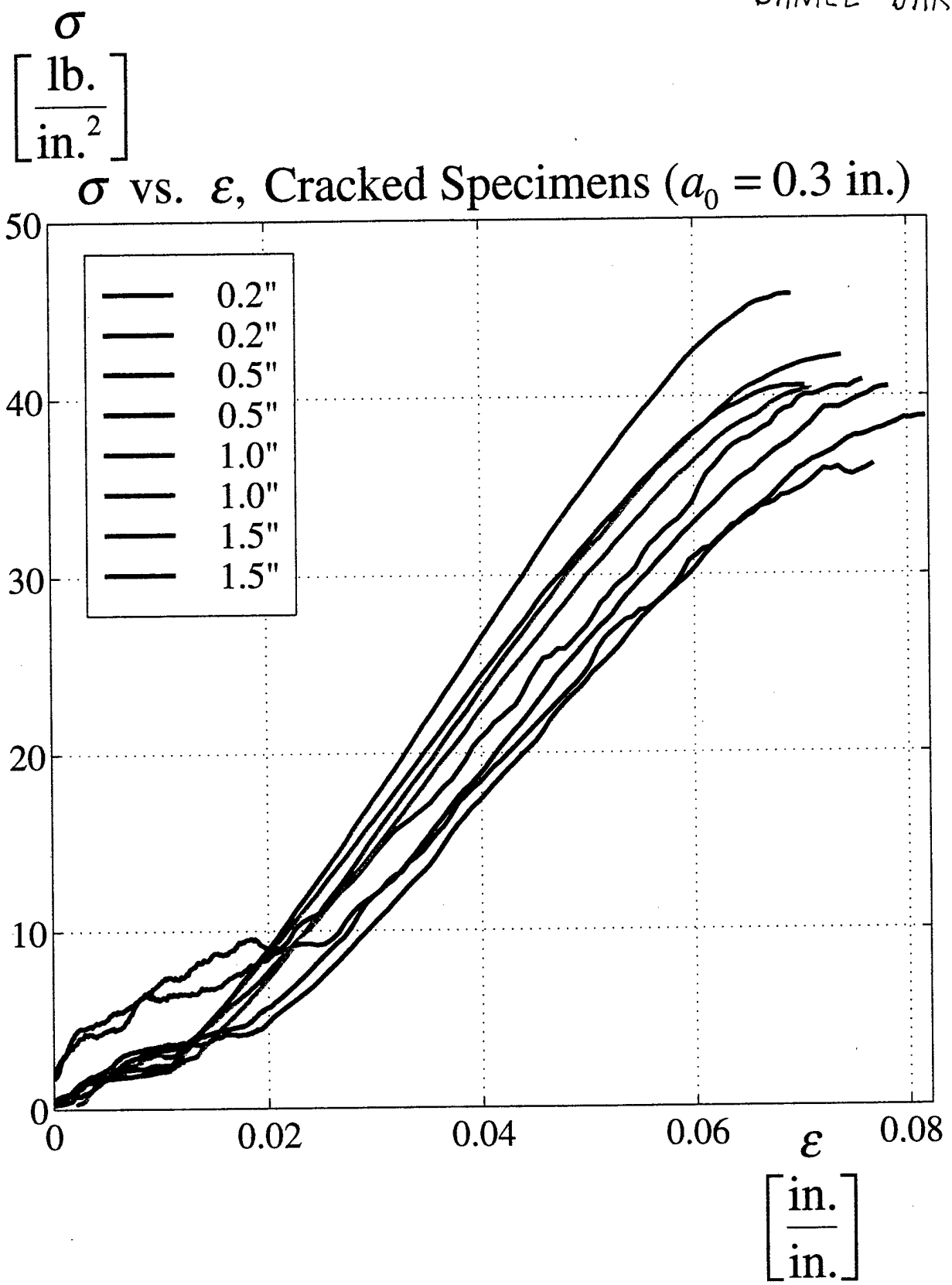
σ
[lb./in.²]
σ vs. ε, Cracked Specimens (a_0 = 0.3 in.)
50
40
30
20
10
0
0
0.02
0.04
0.06
0.08
ε
[in./in.]
0.2"
0.2"
0.5"
0.5"
1.0"
1.0"
1.5"
1.5"

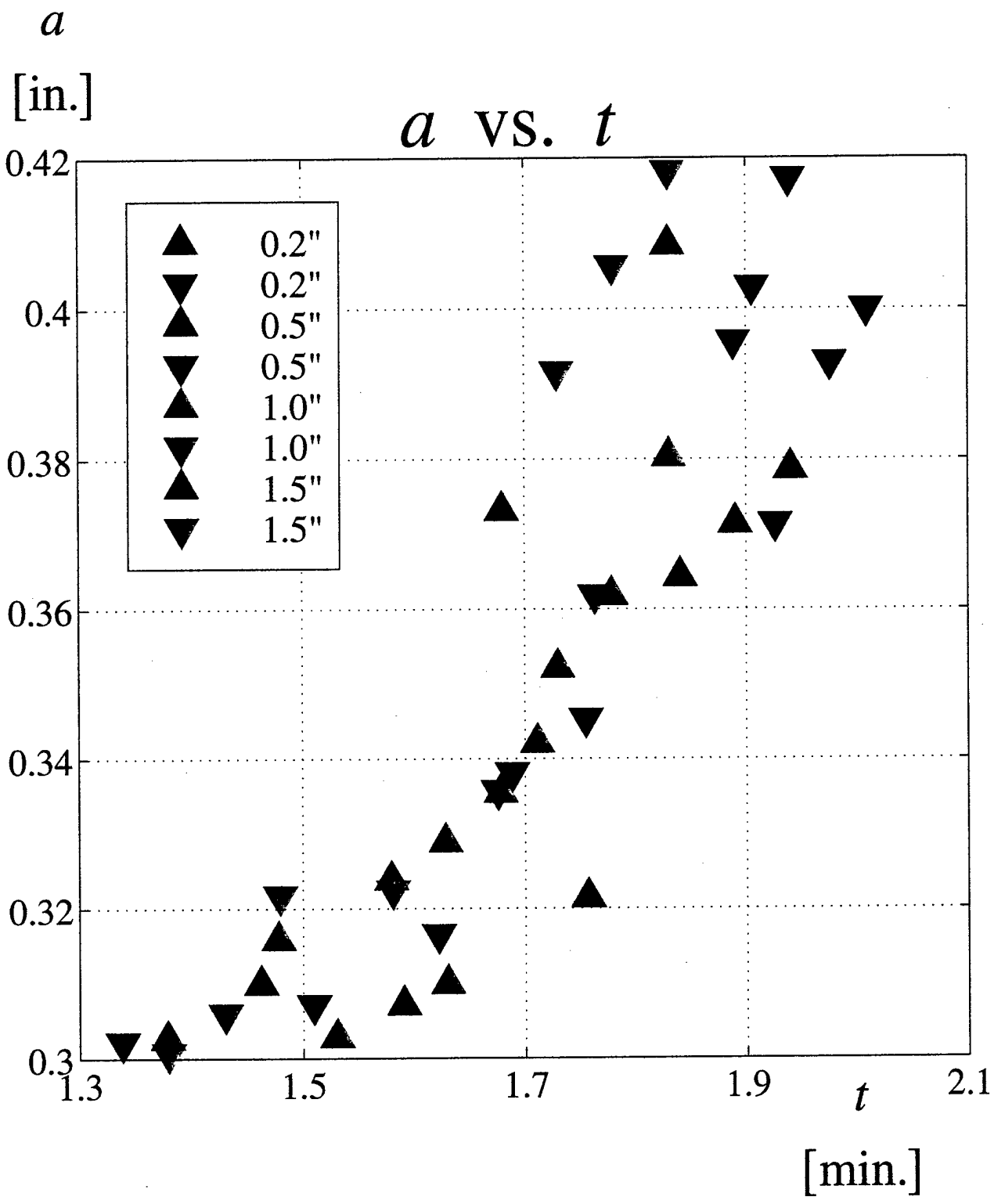
a
[in.]
a vs. t
0.42
0.4
0.38
0.36
0.34
0.32
0.3
1.3
1.5
1.7
1.9
2.1
t
[min.]
0.2"
0.2"
0.5"
0.5"
1.0"
1.0"
1.5"
1.5"

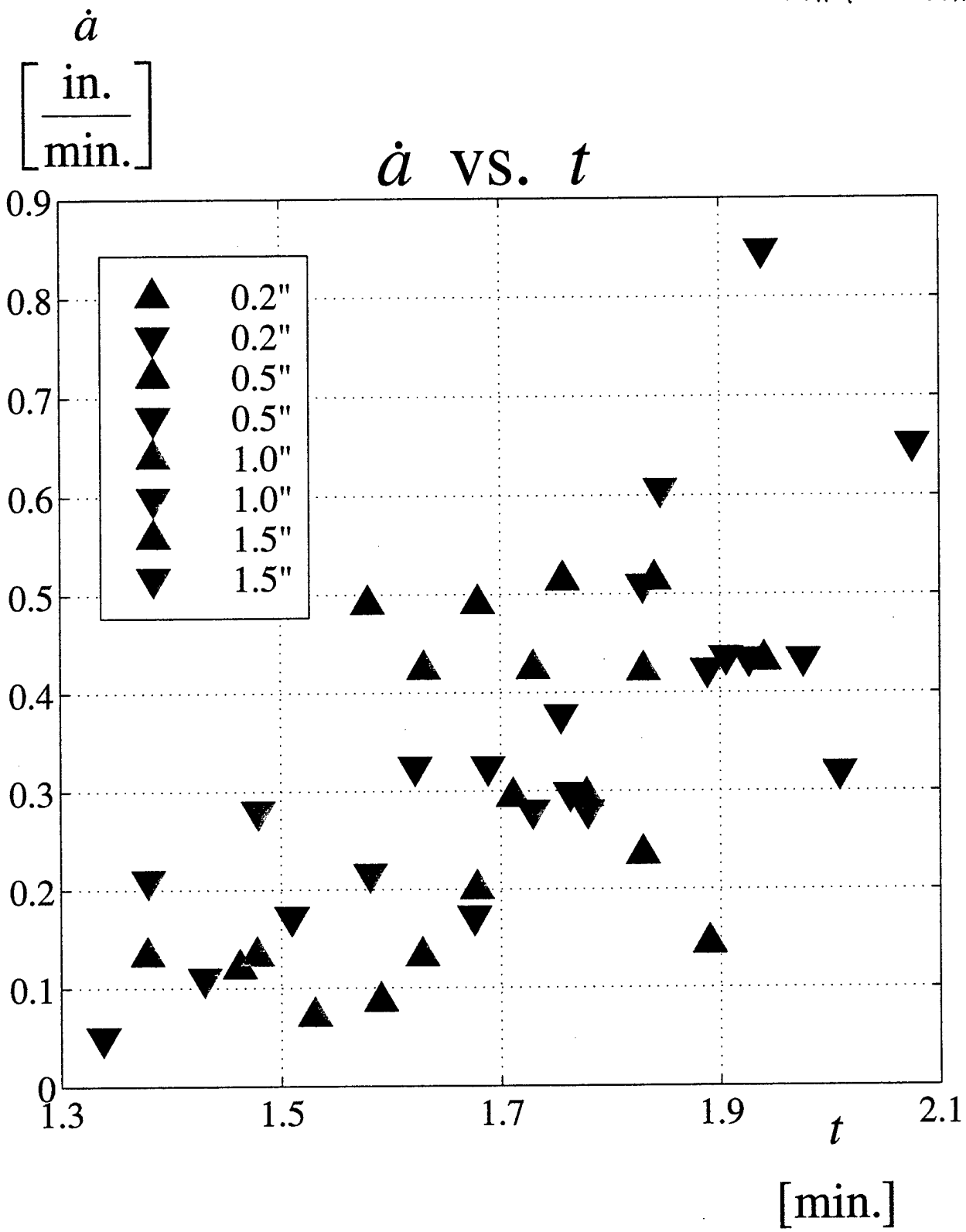
$\dot{a}$ vs. t
$\dot{a}$
$\left[\frac{\text{in.}}{\text{min.}}\right]$
0.2"
0.2"
0.5"
0.5"
1.0"
1.0"
1.5"
1.5"
0.9
0.8
0.7
0.6
0.5
0.4
0.3
0.2
0.1
0
1.3
1.5
1.7
1.9
2.1
t
[min.]

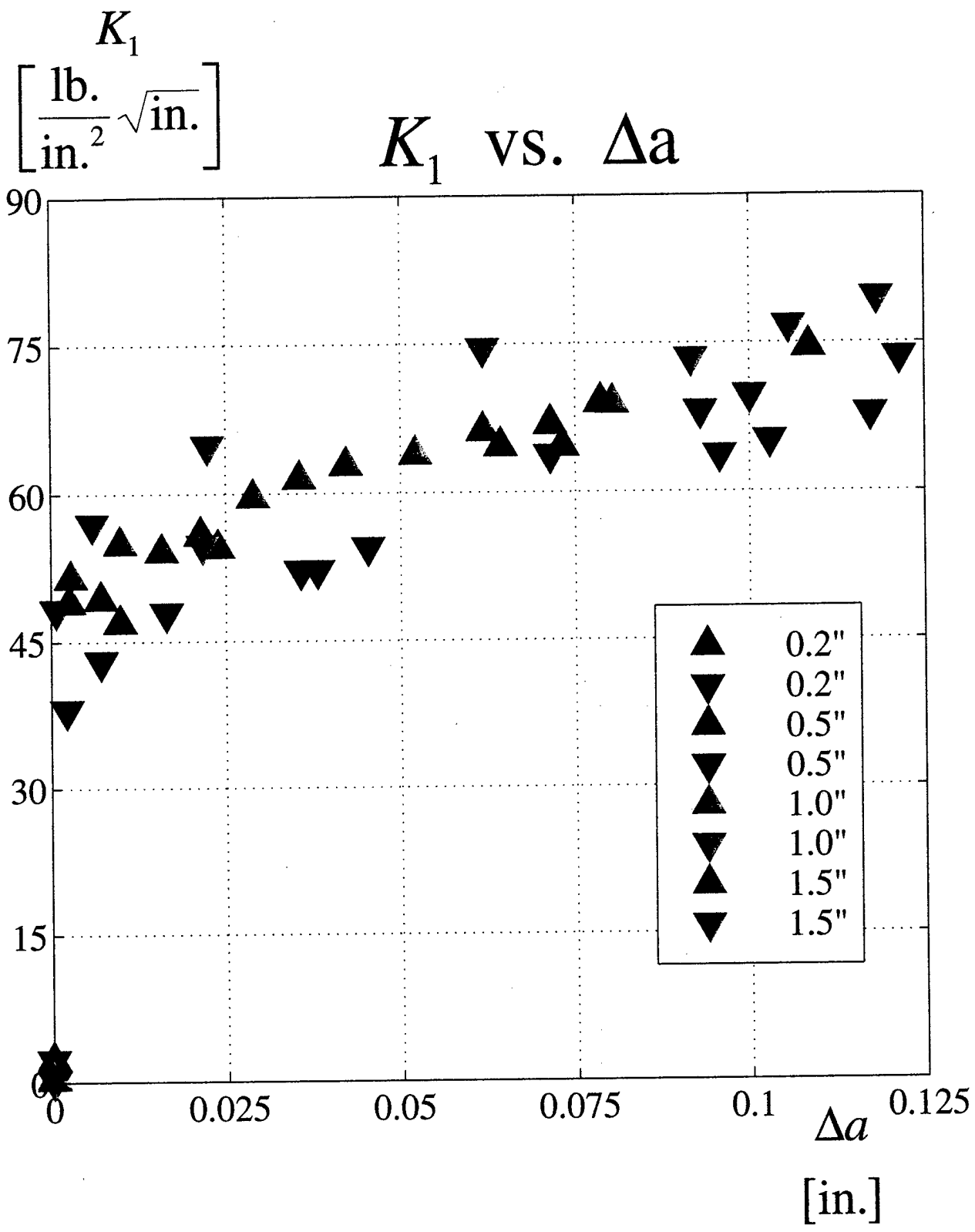
K_1
$\left[\frac{\text{lb.}}{\text{in.}^2}\sqrt{\text{in.}}\right]$
K_1 vs. Δa
90
75
60
45
30
15
0
0
0.025
0.05
0.075
0.1
0.125
Δa
[in.]
0.2"
0.2"
0.5"
0.5"
1.0"
1.0"
1.5"
1.5"

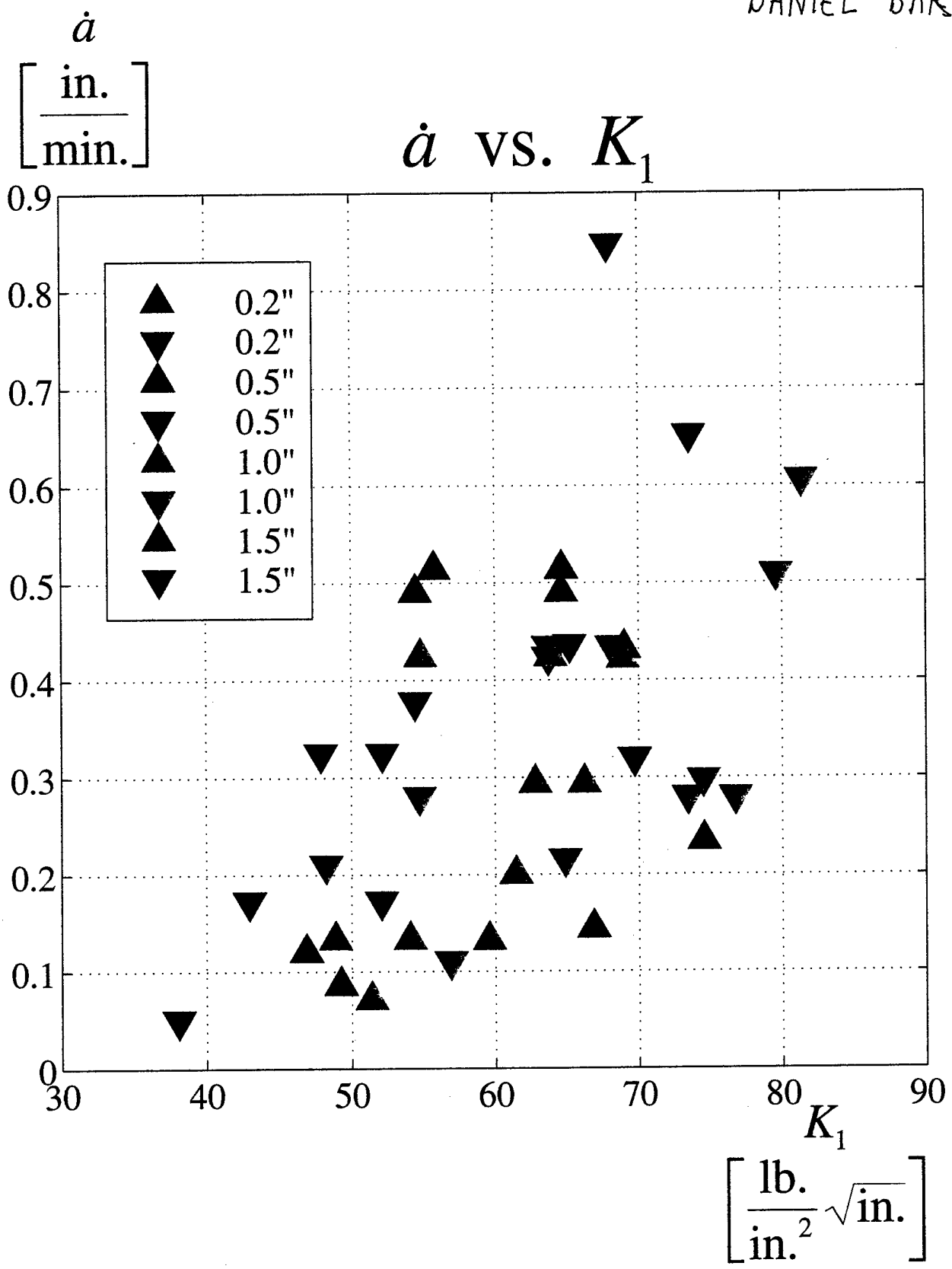
$\dot{a}$ vs. K_1
$\dot{a}$ $\left[\frac{\text{in.}}{\text{min.}}\right]$
0.2"
0.2"
0.5"
0.5"
1.0"
1.0"
1.5"
1.5"
0
0.1
0.2
0.3
0.4
0.5
0.6
0.7
0.8
0.9
30
40
50
60
70
80
90
K_1
$\left[\frac{\text{lb.}}{\text{in.}^2}\sqrt{\text{in.}}\right]$

$\log_{10}(\dot{a})$ vs. $\log_{10}(K_1)$

fit: $\log_{10}(\dot{a}) = -4.580 + 2.256\log_{10}(K_1)$

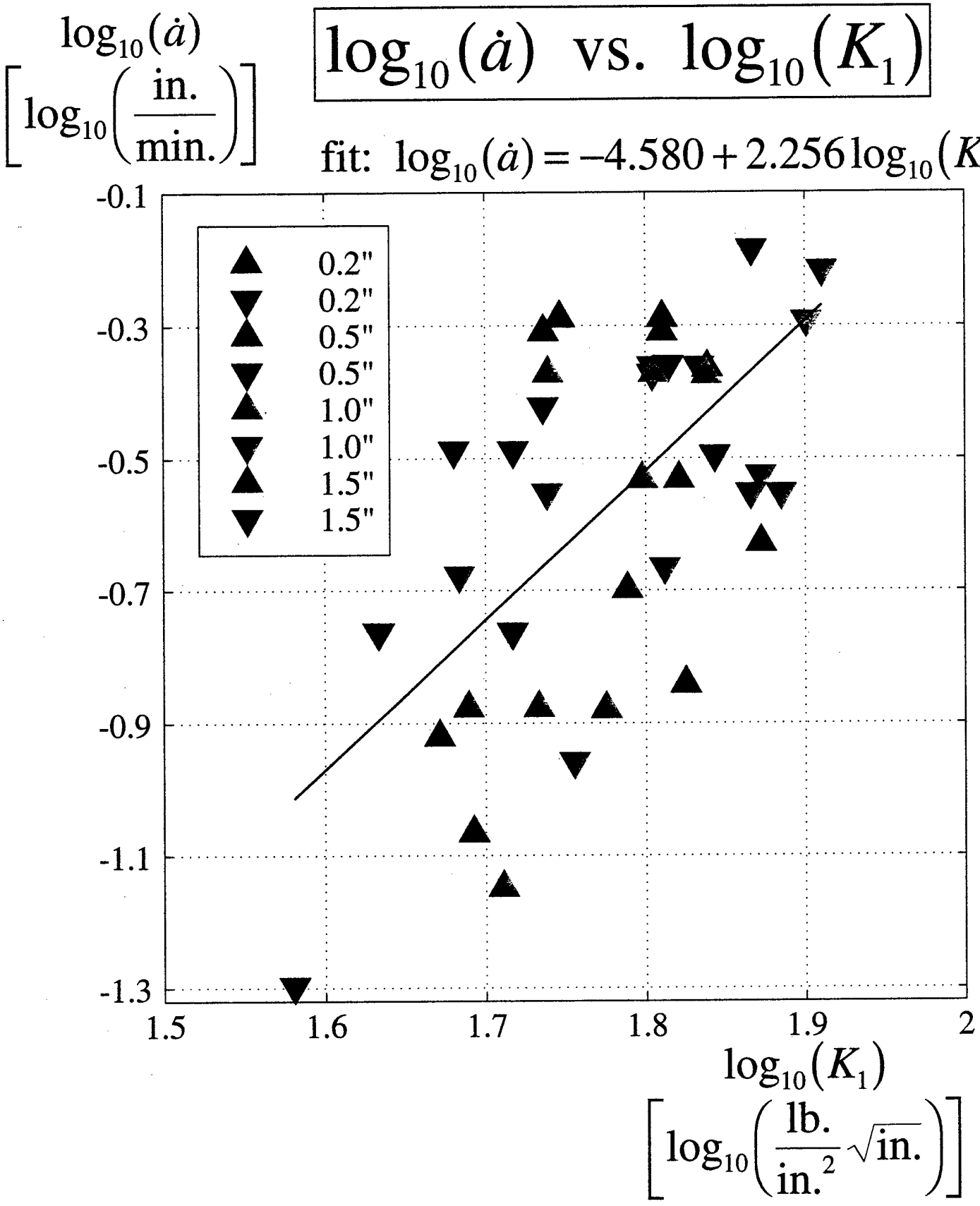

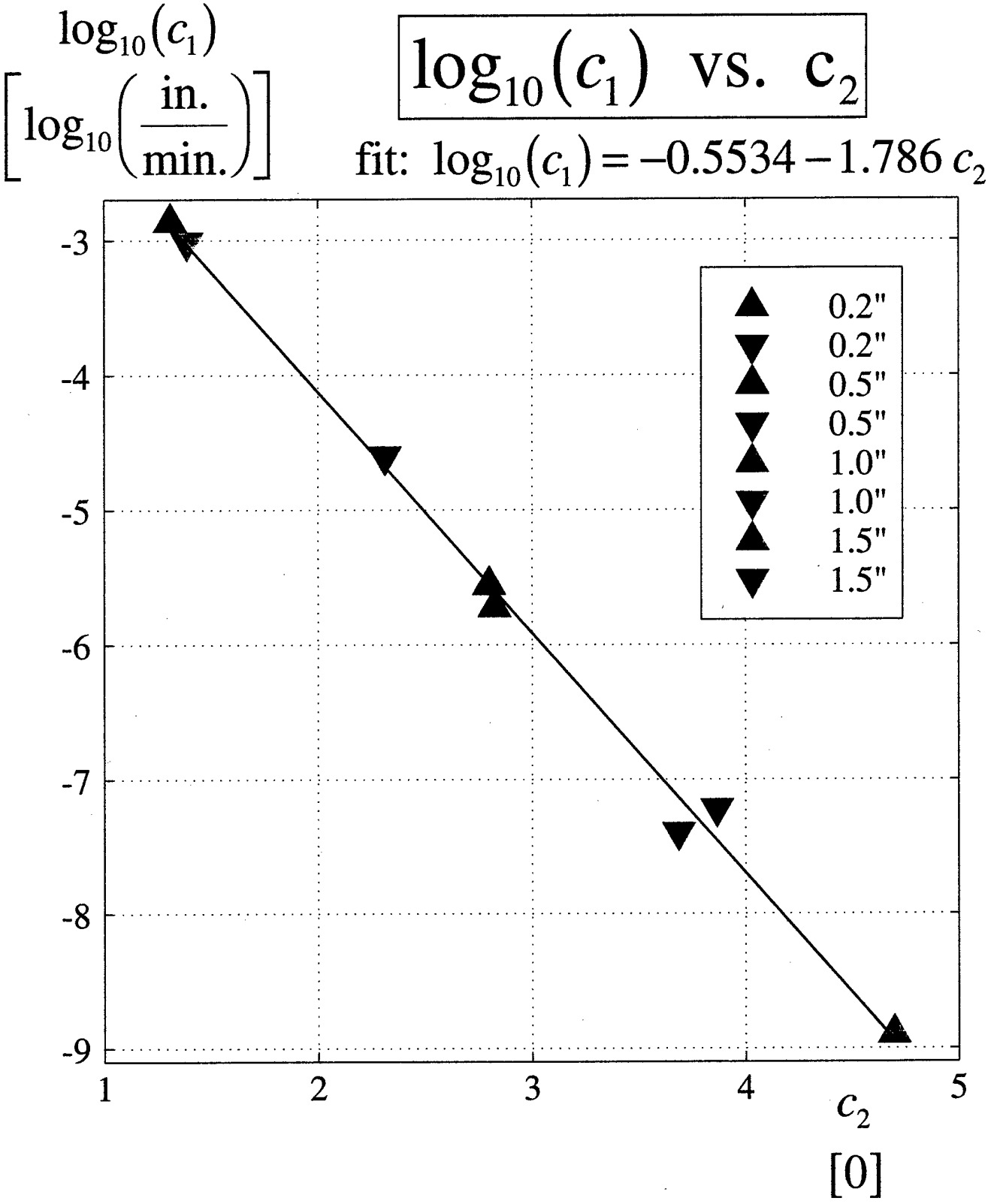
$\log_{10}(c_1)$
$\left[\log_{10}\left(\frac{\text{in.}}{\text{min.}}\right)\right]$
$\log_{10}(c_1)$ vs. c_2
fit: $\log_{10}(c_1) = -0.5534 - 1.786\, c_2$
-3
-4
-5
-6
-7
-8
-9
1
2
3
4
5
c_2
[0]
0.2"
0.2"
0.5"
0.5"
1.0"
1.0"
1.5"
1.5"

Subcritical Crack Growth in a Composite Solid Propellant

D.T. Baron
Raytheon STX Corp.
Edwards AFB, CA 93524

T.C. Miller
Air Force Research Laboratory
Edwards AFB, CA 93524

C.T. Liu
Air Force Research Laboratory
Edwards AFB, CA 93524

Abstract

Uniaxial tension tests using a strain rate of 0.04 in./in./min. are performed on rectangular smooth and single edge-notched specimens of varying thicknesses for a composite solid propellant. Stress-strain, crack growth, crack growth rate and crack growth resistance data are provided. Thickness effects and the mechanism of crack growth are described. Methods of calculation are explained for the crack growth rate and the Mode 1 stress intensity factor. A model is developed for the crack stable growth rate as a function of the stress intensity factor.

Key Words

linear elastic fracture mechanics, LEFM, plane stress, composite solid propellant, crack growth, crack growth rate, mode 1 stress intensity factor, crack growth resistance curve, thickness effect.

Introduction

Composite solid propellants consist of a lightly crosslinked polymer, highly filled with relatively coarse solid particles. They are considered to be incompressible. Their loaded response is viscoelastic. Previous studies have been conducted to investigate crack growth in these materials {1-5}. The basic approach is based on linear elastic or linear viscoelastic fracture mechanics. Experimental results have shown that a power law relationship exists between the crack growth rate ($\dot{a}$) and the Mode 1 (opening mode) stress intensity factor (K_1). This is consistent with the linear viscoelastic fracture theories developed by Knauss {6} and Schapery {7}.

An example of a composite solid propellant can be described as follows {8}. Ammonium perchlorate crystal particles of two sizes, diameters 20μ (1μ = 10^{-6} meter) and 200μ function as the oxidizer. The oxidizer weight fraction for the 20μ particles is 0.3. The oxidizer weight fraction for the 200μ particles is 0.7. Aluminum powder particles of diameter 30μ function as the fuel. Polybutadiene rubber functions as the matrix/binder (also as fuel). The weight fractions for the oxidizer, fuel, and matrix/binder are respectively 0.7, 0.2, 0.1. The specific gravities are respectively 1.69, 2.65, 1.0. The volume fractions are therefore respectively 0.7, 0.13, 0.17. The particle volume fraction (PVF) is 0.83. For every 200μ diameter particle, there are approximately 77 30μ diameter particles, and 429 20μ particles.

For this paper, four different thicknesses (0.2 in., 0.5 in., 1.0 in., 1.5 in.) of smooth and single edge-notched tension (SENT) specimens of a composite solid propellant were uniaxially strained

at a rate ($\dot{\varepsilon}$) of 0.04 in./in./min. The induced end force (F) and crack length (a) (for the SENT specimens) were recorded as functions of $\dot{\varepsilon}$ (equivalently as functions of time, t). Photographs showing the crack growth mechanism are included in the paper, and the mechanism is described. Specimen stress (σ) is plotted versus specimen strain (ε) for both the smooth and notched specimens. $\dot{a}$ is calculated, and a and $\dot{a}$ are plotted versus t. K_1 is calculated and plotted versus the change in the crack length (δa), giving the material's crack growth resistance curve (R-curve). There are plots showing the relationship between $\dot{a}$ and K_1. The $\dot{a}(K_1)$ function is modeled and interpreted. Effects of specimen thickness (b) are noted. Linear elastic fracture mechanics (LEFM) was used. For finite element calculations the state of plane stress was used for all thicknesses. This is because there was no consistent evidence of plane strain, even in the thickest (1.5 in.) specimens, as will be reported. Because of the material's assumed incompressibility, 0.499 was used as the value of Poisson's ratio (ν).

Experiments

All test specimens were rectangular, 1 in. wide (w = 1 in., perpendicular to the direction of loading) and 5 in. long (h = 5 in.). Specimen ends were glued to aluminum tabs and subjected to an applied uniform uniaxial displacement rate ($\dot{\Delta}$) of 0.2 in./min. (applied uniform uniaxial nominal strain rate ($\dot{\varepsilon}$) of 0.04 in./in./min.). Four specimen thicknesses (b) were used, 0.2 in., 0.5 in., 1.0 in., and 1.5 in. Eight unnotched specimens were tested, two of each thickness. The stress (σ) vs. strain (ε) curves for those tests are shown in Figure 7. The average initial (linear) value (E_0) for Young's Modulus is 734 psi. The average maximum average specimen stress ($\sigma_{max.}$) is 90.9 psi, and the average strain at the maximum stress ($\varepsilon(\sigma_{max})$) is 0.187. The average maximum strain ($\varepsilon_{max.}$) is 0.204. The overall trend is for ($\varepsilon_{max.}$) to decrease as b increases. Eight single edge-notched (SENT) specimens were tested (Mode 1 loading), two of each thickness. The notch length (a_0, cut along the specimen width) used was 0.3 in. The σ vs. ε curves for those tests are shown in Figure 8. (σ is calculated using the specimen uncracked cross sectional area, $A = bw$). The curves show small slopes near the origin. This is probably because the specimens were unintentionally put in an initial state of slight compression. The average value for σ_{max} (calculated using $A = bw$) is 40.6 psi. The average value for $\varepsilon(\sigma_{max})$ is 0.075. The overall trend is for Young's Modulus (E) and σ_{max} to increase as b increases.

The plots of Figures 8-14 refer to the eight SENT specimens. In each plot the data shown for a particular specimen stops when failure begins, and therefore corresponds to the strain range $0 \le \varepsilon \le \varepsilon(\sigma_{max})$. This is done so that LEFM can be used. LEFM is not valid once σ begins to decrease as a specimen fails.

Crack Growth Mechanism

The largest particles in a composite solid propellant are typically larger than 100μ (0.1 mm.), so at that scale these materials are non-homogeneous. When stretched, the variations in particle size,

particle distribution, cross link density, and particle-binder bonds result in non-homogeneous stresses and strengths. Because the particles can be considered rigid with respect to the polymer, the magnitudes of local stresses can be much greater than the magnitudes of the applied stresses, particularly when the gaps between particles are small. Because of the randomness of local stresses and strengths, local failure locations usually do not coincide with the points of maximum stress as determined from an elastic analysis for a homogeneous isotropic material. For a cracked specimen, a damage zone forms ahead of the crack tip. Local failures (voids or microcracks) usually occur first in the interior of the damage zone, not at the crack tip itself. The crack tip extends into the damage zone when the ligament of material separating it from the nearest void or microcrack breaks. The front of the void or microcrack becomes the new crack tip. As the crack tip extends, the damage zone moves forward, gaining new material. The type of damage which causes void formation is matrix/binder cracking. The types of damage which cause damage zone microcracking are particle-matrix/binder debonding (dewetting) and particle cracking.

Figures 1-6 show photographs of crack growth in the SENT specimens. All four specimen thicknesses (0.2 in., 0.5 in., 1.0 in., 1.5 in.) are shown, and the common growth mechanism is void formation in the damage zone ahead of the crack tip, and then crack tip extension due to ligament rupture. This type of growth produces the rough crack surfaces shown in Figures 3-6. Figures 1 and 2 show crack initiation from an initial notch. Crack tip blunting occurs before initiation because of the large uniaxial strain (Figure 7) the material is capable of withstanding.

Examinations of the SENT specimen fracture surfaces showed, that for all thicknesses the crack fronts were straight lines and perpendicular to the direction of crack growth. This implies that the region near the crack tip always experienced a state of plane stress. If plane strain existed, it would have been indicated in the thicker specimens by a curved crack front which was advanced farther near its middle, and less near its edges. In that case the interior of the crack tip region would be in plane strain and the exterior would be in plane stress. (A material's crack growth resistance is less in plane strain than in plane stress). Apparently, void formations in the damage zone prevented the lateral constraint which is necessary for a state of plane strain.

Calculation of the Crack Growth Rate

The rates ($\dot{a}$) of crack growth (for $n+1$ points (a, t) numbered 0, 1, ..., n) were calculated by

$$\dot{a}(0) = \frac{a(1)-a(0)}{t(1)-t(0)}$$

$$\dot{a}(i) = \max\left(\frac{a(i)-a(i-1)}{t(i)-t(i-1)}, \frac{a(i+1)-a(i)}{t(i+1)-t(i)}\right). \qquad (1)$$

$$\dot{a}(n) = \frac{a(n)-a(n-1)}{t(n)-t(n-1)}$$

This method is easy to implement, and assigns each experimental point (a, t) a value of $\dot{a}$. The values of $\dot{a}$ are not smoothed. Each interior point (a, t) is assigned the larger of the two adjacent calculated values. Using the method results in the ability to determine the most conservative

upper bound on the envelope of $\dot{a}$ for the set of SENT specimens.

The Experimental Crack Growth Rate

Figure 9 shows a plot of crack length (a) vs. time (t). The crack initiation time (t_c) varies from 1.34 min. to 1.59 min. The average value for t_c is 1.45 min. The corresponding applied nominal strain at crack initiation $(\varepsilon_c = t_c \cdot \dot{\varepsilon})$ varies from 0.0535 to 0.0636. The average value for ε_c is 0.0581. The maximum recorded value for a is 0.427 in. Figure 10 shows a plot of crack growth rate $(\dot{a})$ vs. time. The maximum calculated value for $\dot{a}$ is 0.847 in./min., approximately 4.2 times the applied displacement rate of $\dot{\Delta} = 0.2$ in./min.

Calculation of the Mode 1 Stress Intensity Factor

For the SENT experiments, a specimen's edge displacement (Δ) was prescribed as a function of time (t). The crack length (a), was measured as a function of t. For each point (Δ, a) of each specimen thickness (b), the LEFM Mode 1 stress intensity factor (K_1) was calculated by the method described in this section.

K_1 can be written in the form

$$K_1 = \sigma_\infty^{\text{avg.}} \sqrt{w} f\left(\frac{a}{w}, \frac{h}{w}\right), \tag{2}$$

where $\sigma_\infty^{\text{avg.}}$ is the average value of the specimen edge stress (σ_∞) induced by the application of the uniform edge displacement (Δ); w is the specimen width, h is the specimen length, and f is some function of a/h and h/w. Dividing K_1 by $\sigma_\infty^{\text{avg.}} \sqrt{a}$ gives

$$\frac{K_1}{\sigma_{\text{avg.}} \sqrt{a}} = \sqrt{\frac{w}{a}} f\left(\frac{a}{w}, \frac{h}{w}\right), = g\left(\frac{a}{w}, \frac{h}{w}\right), \tag{3}$$

where g is a second function of a/h and h/w. According to LEFM, the energy release rate (J) (for plane stress) can be expressed as

$$J = \frac{K_1^2}{E}, \tag{4}$$

where E is Young's Modulus. (For the case of plane strain, in Equation 4, $E \rightarrow E/(1-\nu^2)$.) This implies that

$$K_1 = \sqrt{JE}. \tag{5}$$

$\sigma_\infty^{\text{avg.}}$ can be expressed as

$$\sigma_\infty^{\text{avg.}} = \frac{F}{A}, \tag{6}$$

where F is the end force induced on the specimen, and A is the specimen's uncracked cross-sectional area (bw). Therefore $\sigma_\infty^{\text{avg.}}$ becomes

$$\sigma_\infty^{\text{avg.}} = \frac{F}{bw}. \tag{7}$$

Using Equations 5 and 7 in Equation 3 gives

$$\frac{K_1}{\sigma_\infty^{\text{avg.}}\sqrt{a}} = g\left(\frac{a}{w}, \frac{h}{w}\right), = \frac{bw}{F}\sqrt{\frac{JE}{a}}. \tag{8}$$

The function $g\left(\frac{a}{w}, \frac{h}{w}\right)$ is the specimen geometry correction factor for stress intensity, and is approximated by numerically calculating $\frac{bw}{F}\sqrt{\frac{JE}{a}}$. Linear elastic plane stress finite element calculations (ABAQUS code) were performed of a SENT specimen subjected to a uniform uniaxial displacement (Δ), using $w = 1$ and $h = 5$. The value of the specimen thickness (b) does not appear in plane finite element calculations, and is implicitly equal to 1. (Note that the value of g is independent of the value of the prescribed displacement (Δ) used in a finite element calculation. Note also that although E appears in the expression $\left(\frac{bw}{F}\sqrt{\frac{JE}{a}}\right)$ for g, the value of the expression is independent of the value of E used. Any (positive) values can be used for Δ and E in the finite element calculations. The value of g depends only on the two parameters a/w and h/w.) The value of a was varied, and one finite element calculation was performed for each value. Each finite element calculation output a value for F and a value for J (energy domain integral method). g was plotted versus a/w. A second order polynomial was fitted to g,

$$g\left(\frac{a}{w}, \frac{h}{w} = 5\right) \cong p_0 + p_1\frac{a}{w} + p_2\left(\frac{a}{w}\right)^2, \tag{9}$$

giving a close approximation to the function. From Equation 8,

$$K_1(\Delta, a, b, w, h) = \sigma_\infty^{\text{avg.}} \sqrt{a} \cdot g\left(\frac{a}{w}, \frac{h}{w}\right). \tag{10}$$

Using Equations 7 and 9 in Equation 10 gives

$$K_1(\Delta, a, b, w, h = 5) = \frac{F\sqrt{a}}{bw} \cdot \left(p_0 + p_1\frac{a}{w} + p_2\left(\frac{a}{w}\right)^2\right). \tag{11}$$

For each experimental point (Δ, a) of each specimen thickness (b), $K_1(\Delta, a, b, w = 1)$ was determined using Equation 11, in which F was the experimentally measured specimen end force associated with (Δ, a).

The alternative "brute force" method for calculating K_1 is to make one finite element calculation for each experimental point (Δ, a) of each specimen thickness (b), in order to find J for the point, and then to compute K_1 with Equation 5, using $E = E_0$. The advantage of using the method of this section is that once the approximating function of Equation 9 is determined, K_1 can be found for any number of points (Δ, a) without doing more finite element calculations. Each finite element calculation of J is not trivial with respect to the number of elements required to obtain a reasonably accurate result. When determining the function g of Equation 8, only enough points were (finite element) calculated to provide the function's shape.

This paragraph is a clarification of the previous statement that g depends only on the two parameters a/w and h/w. The experimental SENT specimens were symmetric with respect to geometry and loading, about the crack. So for the finite element calculations, one half of a specimen was modeled, cut thru the crack centerline. The mesh boundary along the crack centerline was referred to as the bottom. The points of the mesh bottom boundary which were ahead of the crack tip were constrained from movement in the y (perpendicular to the crack) direction. The displacement Δ was applied in the y direction to each point on the mesh top boundary. The ends of the experimental specimens were glued to aluminum end tabs. In order to simulate the glued condition, each point of the mesh top boundary was constrained from movement in the x direction. For this case, in which the simulated specimen is prevented from free lateral contraction, the induced stress distribution in the interior and on the boundaries of the specimen, is some unknown nonlinear function of position (x, y) and of Poisson's ratio (ν), i.e., $\sigma = \sigma(x, y, \nu)$. This results in g at any point being dependent on the value of ν. (This effect of ν on g also exists if load is applied to the specimen by prescribing tractions.) Since g depends on ν, g is also dependent on whether plane stress or plane strain is used. The influence of the value of ν on the value of g increases primarily with decreasing h/w, and secondarily with decreasing a/w. As h/w increases, g becomes independent of the value ν, and also of the type of loading (prescribed uniform edge displacement or prescribed uniform edge stress). The finite element

calculations of g which were made for the experimental specimens of this paper can be confidently applied only for the particular case of a plane stress SENT specimen with $\nu = 0.499$ and $h/w = 5$, subjected to prescribed uniform edge displacement. There is no way to convert these values of g to a different case.

The Crack Growth Resistance Curve

Figure 11 is a plot of K_1 vs. the change in the crack length (δa). These curves are called crack growth resistance curves (R-curves), and are a measure of a material's resistance to crack growth. The average value of K_1 at crack initiation (K_{1c}) is 47.8 lb. / in.$^{1.5}$. The maximum value recorded for K_1 is 81.4 lb. / in.$^{1.5}$. The condition $K_1 < K_{1c}$ corresponds to crack tip blunting, as is shown in Figure 1. The overall trend is for K_{1c} to increase with increasing b. (This trend provides additional evidence that the thicker specimens were not in a state of plane strain. If it is assumed that as a specimen's thickness (b) is increased, the state of the crack tip region transitions from plane stress to plane strain, then K_{1c} should decrease with increasing b, because a material's crack growth resistance is smaller in plane strain than in plane stress.)

Analysis of the Crack Growth Rate

Figure 12 shows a plot of $\dot{a}$ vs. K_1. The distribution of the points suggest the use of a parabolic modeling function. According to Knauss {6}, and Schapery {7}, the crack growth rate for a SENT specimen of a linearly viscoelastic material can be expressed as

$$\dot{a} = c_1 K_1^{c_2}. \tag{12}$$

(Note that in Equation 12, c_1 and c_2 are not asserted to be material properties, but rather are assumed to be specimen dependent.) Therefore,

$$\log_{10}(\dot{a}) = \log_{10}(c_1) + c_2 \log_{10}(K_1). \tag{13}$$

Figure 13 shows a plot of $\log_{10}(\dot{a})$ vs. $\log_{10}(K_1)$. Also shown is a least squares linear curve fit, giving (for $[\dot{a}]$ = in. /min., $[K_1]$ = lb. /in.$^{1.5}$, ($[x] \equiv$ "units of x"))

$$\log_{10}(\dot{a}) = -4.58 + 2.26 \log_{10}(K_1). \tag{14}$$

Therefore, the best fit pair (c_1, c_2) for representing all eight SENT specimens is $(10^{-4.58}, 2.26)$. Equation 12 can then be written

$$\dot{a} = 2.63 \times 10^{-5} K_1^{2.26} \quad \text{in./min.} \tag{15}$$

It was observed that c_1 and c_2 are not independent parameters. Figure 14 shows a plot of $\log_{10}(c_1)$ vs. c_2 (one best fit pair (c_1, c_2) is calculated for each of the eight SENT specimens). Also shown is a least squares linear curve fit, giving,

$$\log_{10}(c_1) = -0.553 - 1.79c_2. \tag{16}$$

Substituting Equation 16 into Equation 12 eliminates c_1 and gives

$$\dot{a} = 0.280 \cdot (0.0164K_1)^{c_2} \quad \text{in./min.} \tag{17}$$

c_2 can be solved for, giving

$$c_2 = \frac{\log_{10}(\dot{a}) + 0.554}{\log_{10}(K_1) - 1.79}. \tag{18}$$

Equation 18 indicates that for a particular SENT specimen, any experimental point $(K_1, \dot{a})$ should give an estimate for the parameter c_2 for that specimen.

Substituting Equation 16 into Equation 13 and rearranging gives

$$\log_{10}(\dot{a}) + 0.553 = c_2 \cdot (\log_{10}(K_1) - 1.79). \tag{19}$$

Equation 19 has the form of a line, i.e.,

$$y - y_1 = m \cdot (x - x_1). \tag{20}$$

Therefore, Equation 16 is identically satisfied for any line which passes thru the point $(\log_{10}(K_1) = 1.79,\ \log_{10}(\dot{a}) = -0.553)$, and has some slope c_2. This means any line passing thru the point $(1.79, -0.553)$. If Equation 16 was exactly true (if each point in Figure 14 was exactly on the line), then in Figure 13 the shown line (which is the best fit for the aggregate of the specimens) would pass thru the point $(1.79, -0.553)$. Also if Equation 16 was exactly true, then in Figure 13 if a best fit line was plotted for each specimen, all of those lines would pass thru the point $(1.79, -0.553)$. Therefore, point $(1.79, -0.553)$ can be designated the "pivot point" for line fits of specimen experimental data of $\log_{10}(\dot{a})$ vs. $\log_{10}(K_1)$.

Each point $(\log_{10}(c_1), c_2)$ in Figure 14 was determined by calculating a best fit line thru the points $(\log_{10}(K_1), \log_{10}(\dot{a}))$ for the particular specimen. Then the relation of Equation 16 was determined by calculating a best fit line thru all of the points $(\log_{10}(c_1), c_2)$. The relation of

Equation 14 was determined by calculating a best fit line thru the points $(\log_{10}(K_1), \log_{10}(\dot{a}))$ for all of the specimens together. From Equation 14, $\log_{10}(c_1) = -4.58$. If c_2 from Equation 14 ($c_2 = 2.26$) is substituted into Equation 16, then $\log_{10}(c_1) = -4.60$. The two values of $\log_{10}(c_1)$ vary by 0.4%. Their agreement is good because each point in Figure 14 is close to the fit line.

Equation 17 can be written in the form

$$\dot{a} = c_3 \cdot (c_4 K_1)^{c_2} \text{ in./min.,} \tag{21}$$

with $c_3 = 0.280$ and $c_4 = 0.0164$. c_3 and c_4 are independent of specimen thickness (b), and are constants for this particular composite solid propellant, and the particular values for the specimen width ($w = 1$ in.), specimen length ($h = 5$ in.), notch length (or initial crack length, $a_0 = 0.3$ in.), and applied strain rate ($\dot{\varepsilon} = 0.04$ in./in./min.). c_2 is a variable, dependent on the specific randomness of a particular specimen. Equation 21 is only approximately true, because Equation 16 is only approximately true. For an actual specimen, when K_1 equals K_{1c}, then $\dot{a}$ equals 0. In order for Equation 21 to approximate this condition, c_2 should increase as K_{1c} increases. For any value of c_2, a curve having the form of Equation 21 will pass thru the common intersection point $\left(K_1 = \frac{1}{c_4}, \dot{a} = c_3\right)$. The common intersection point for best fit (to determine c_2) curves of each of the eight SENT specimens represented in Figure 12 would be ($K_1 = 61.0$ lb. $\div$ in.$^{1.5}$, $\dot{a} = 0.280$ in./min.). At the common intersection point, the slope of the function of Equation 21 is linearly proportional to c_2, and therefore increases with K_{1c} (because c_2 increases with K_{1c}). This means that at the common intersection point, the rate of change of $\dot{a}$ with respect to K_1, increases as K_{1c} increases.

Conclusions

Constant uniaxial strain rate tests were performed on four thicknesses (0.2 in., 0.5 in., 1.0 in., 1.5 in.) of specimens of a particular composite solid propellant. Tests were performed on eight smooth (unnotched) specimens to determine the material's uniaxial stress-strain behavior. Tests were performed on eight single edge-notched tension (SENT) specimens to determine cracked uniaxial stress-strain behavior, the material's Mode 1 crack growth resistance, and to determine and model the crack growth rate ($\dot{a}$). Methods were described for calculating $\dot{a}$ from crack growth data, and for calculating the Mode 1 stress intensity factor (K_1). For all analysis, linear elastic fracture mechanics (LEFM) was used. Results showed that there were no consistent and significant effects of specimen thickness (b). The crack growth data made it seem likely that for all four values of b, the crack tip region experienced a state of plane stress. This was explained as

being due to void formations in the crack tip damage zone preventing the lateral constraint which would otherwise produce a state of plane strain in a thicker specimen. The crack growth rate was modeled as $\dot{a} = c_1 K_1^{c_2}$. c_1 and c_2 were assumed to be mutually independent of each other, and to individually depend on the specific randomness of a particular specimen. Then data showed that c_1 and c_2 were mutually dependent, and one could be eliminated. The crack growth rate could then be modeled as $\dot{a} = c_3 \cdot (c_4 K_1)^{c_2}$. c_3 and c_4 were independent of b, and depended on the particular material, and the particular values for the specimen width (w = 1 in.), specimen length (h = 5 in.), notch length (a_0 = 0.3 in.), and applied strain rate ($\dot{\varepsilon}$ = 0.04 in./in./min.). So c_3 and c_4 were constants for the eight SENT specimens. c_2 depended on the specific randomness of a particular specimen. It was noted that all SENT specimen curve fits (to determine c_2) of $\dot{a} = c_3 \cdot (c_4 K_1)^{c_2}$ would pass thru the common point ($K_1 = 1/c_4, \dot{a} = c_3$), and at that point the rate of change of $\dot{a}$ with respect to K_1 would increase with increasing values of K_{1c}.

References

{1} Liu, C.T., 'Crack growth behavior in a composite propellant with strain gradients - Part II', *Journal of Spacecraft and Rockets*, 27, 1990, 647-652.

{2} Liu, C.T., 'Crack propagation in a composite solid propellant', *Proceedings of the 1990 SEM Spring Conference*, Baltimore MD, 1990, 614-620.

{3} Smith, C.W., L. Wang, H. Mouille, and C.T. Liu, 'Near tip behavior of a particulate composite material containing cracks at ambient and elevated temperatures', ASTM STP 1189, 1993, 775-787.

{4} Liu, C.T. and C.W. Smith, 'Temperature and rate effects on stable crack growth in a particulate composite material', *Proceedings of the 1994 SEM Spring Conference*, Baltimore MD, 1994, 146-149.

{5} Liu, C.T., 'Numerical modeling of crack-defect interaction', *Journal of Propulsion and Power*, 7, 1991, 526-530.

{6} Knauss, W.G., 'On the steady propagation of a crack in a viscoelastic sheet: Experiments and analysis', *Deformation and Fracture of High Polymers*, H. Henning Kausch, J.A. Hassell and R.I. Jaffee (eds.), Plenum Press, New York, 1974, 501-541.

{7} Schapery, R.A., 'A theory of crack initiation and growth in viscoelastic media I', *International Journal of Fracture Mechanics*, 11, 1975, 141-159.

{8} Sutton, G.P., *Rocket Propulsion Elements - An Introduction to the Engineering of Rockets*, 5th ed., John Wiley & Sons, New York, 1986, 292-316.

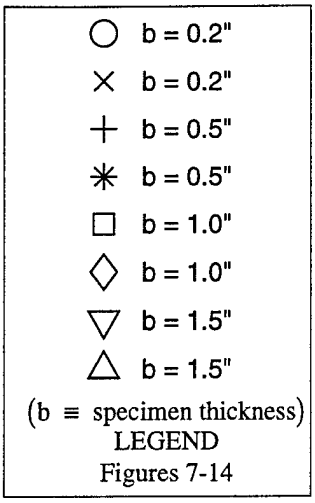

Figures 7-14

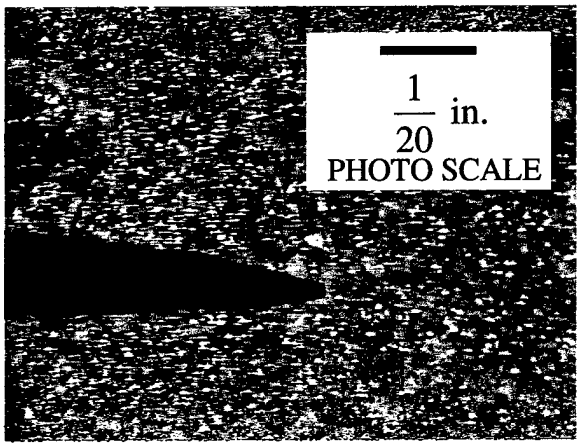

Figure 1. b = 1.0 in., Crack Tip Blunting

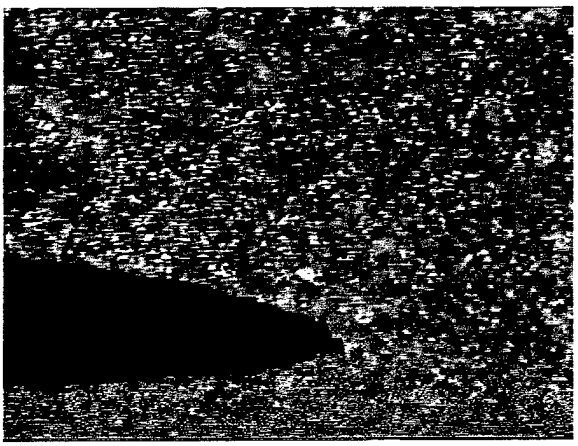

Figure 2. b = 1.0 in., Initial Crack Growth

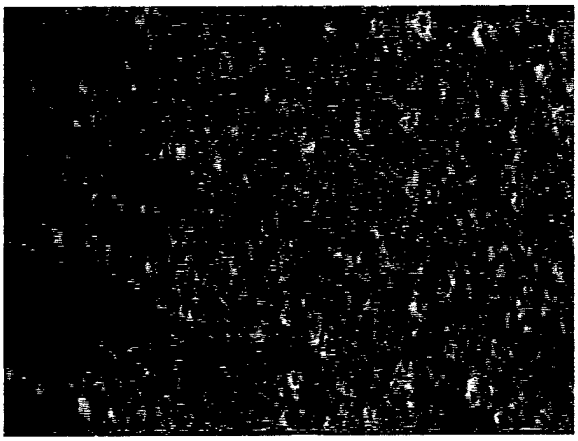

Figure 3. b = 1.5 in., Damage Formation

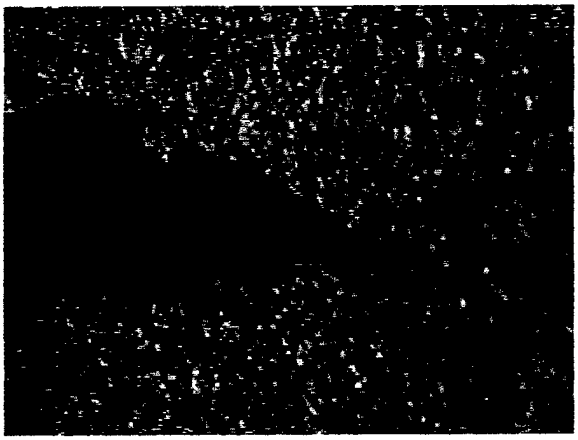

Figure 4. b = 0.2 in., Damage Zone Voids

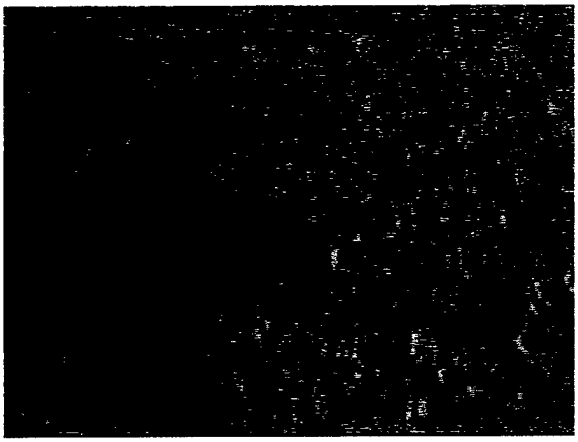

Figure 5. b = 0.2 in., Single Ligament

Figure 6. b = 0.5 in., Double Ligament

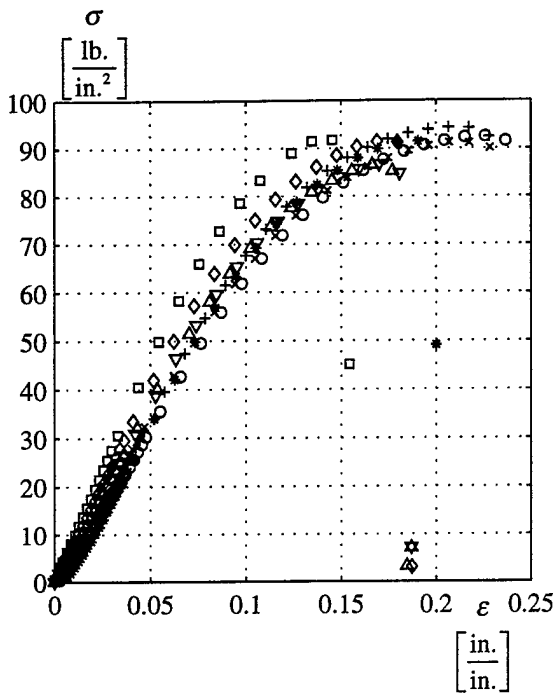

Figure 7. σ vs. ε, Uncracked Specimens ($a_0 = 0$)

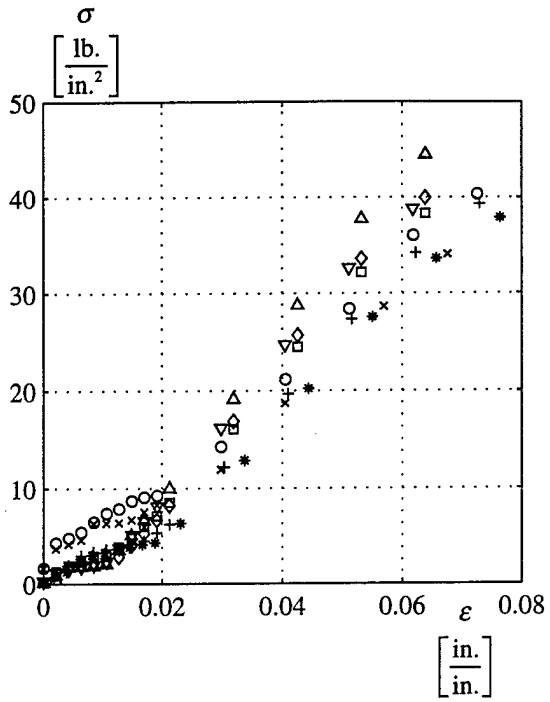

Figure 8. σ vs. ε, Cracked Specimens (a_0 = 0.3 in.)

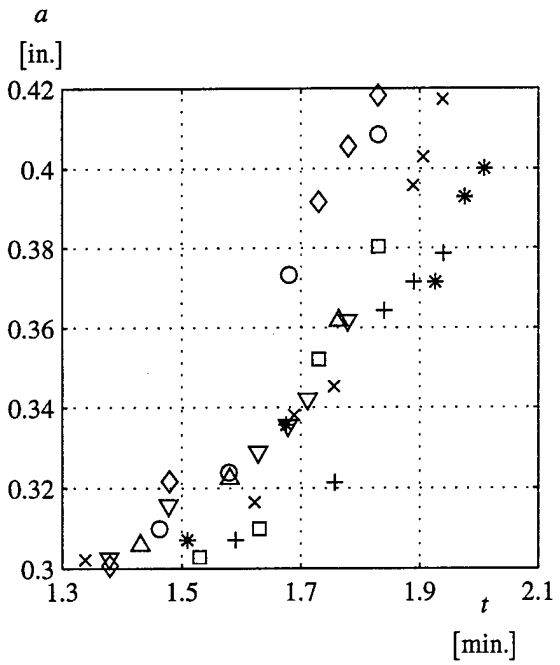

Figure 9. a vs. t

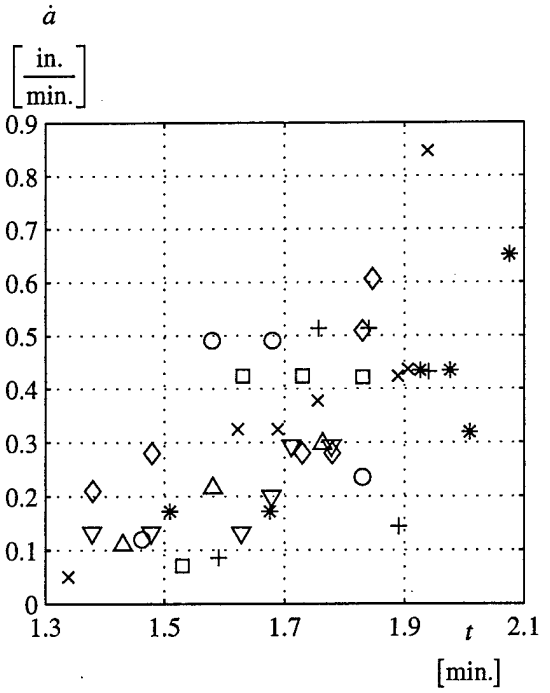

Figure 10. $\dot{a}$ vs. t

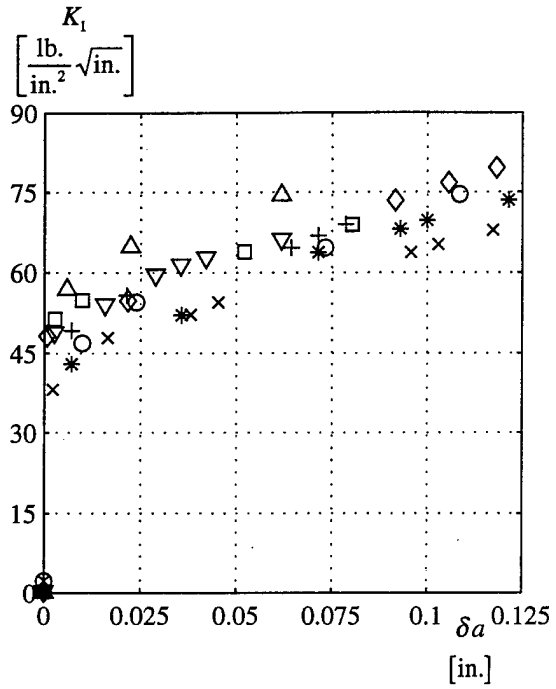

Figure 11. K_1 vs. δa

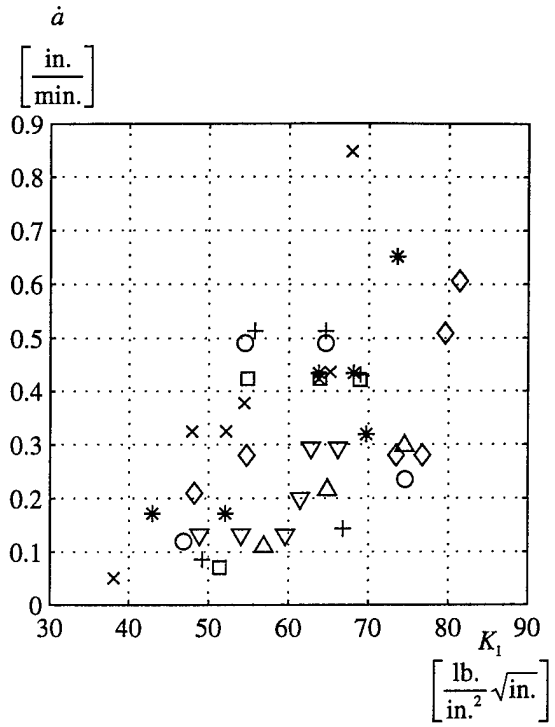

Figure 12. $\dot{a}$ vs. K_1

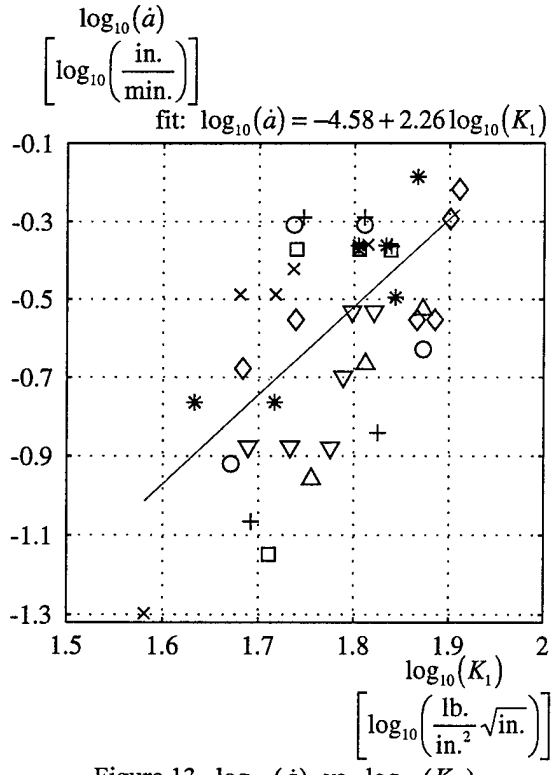

Figure 13. $\log_{10}(\dot{a})$ vs. $\log_{10}(K_1)$

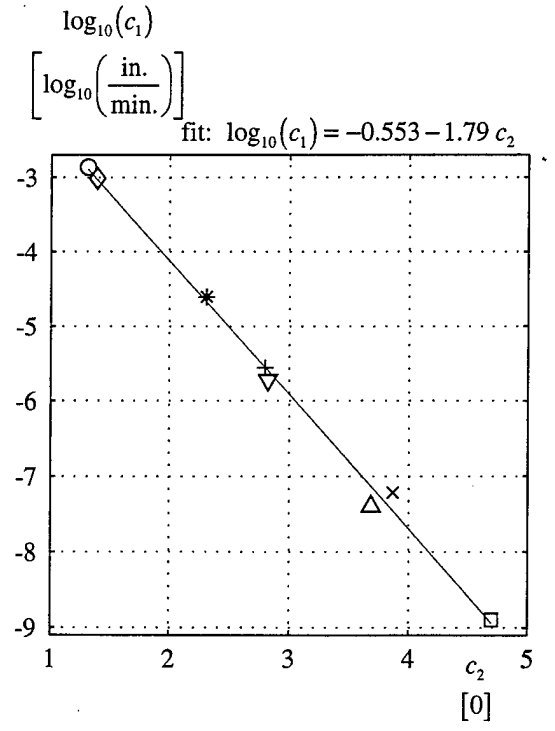

Figure 14. $\log_{10}(c_1)$ vs. c_2